
















The Hourglass Simulation: A Catalog for the *Roman* High-Latitude Time-Domain Core Community Survey

B. M. ROSE ¹ M. VINCENZI ^{2,3,*} R. HOUNSELL ^{4,5} H. QU ⁶ L. ALDOROTY ³ D. SCOLNIC ³ R. KESSLER ^{7,8}
P. MACIAS ⁹ D. BROUT ¹⁰ M. ACEVEDO ³ R. C. CHEN ³ S. GOMEZ ¹¹ E. PETERSON ³ D. RUBIN ^{12,13}
AND M. SAKO ⁶

THE ROMAN SUPERNOVA PROJECT INFRASTRUCTURE TEAM

¹*Department of Physics and Astronomy, Baylor University, One Bear Place #97316, Waco, TX 76798-7316, USA*

²*Department of Physics, University of Oxford, Denys Wilkinson Building, Keble Road, Oxford OX1 3RH, United Kingdom*

³*Department of Physics, Duke University, Durham, NC 27708, USA*

⁴*University of Maryland, Baltimore County, Baltimore, MD 21250, USA*

⁵*NASA Goddard Space Flight Center, Greenbelt, MD 20771, USA*

⁶*Department of Physics and Astronomy, University of Pennsylvania, 209 South 33rd Street, Philadelphia, PA 19104, USA*

⁷*Department of Astronomy and Astrophysics, University of Chicago, Chicago, IL 60637, USA*

⁸*Kavli Institute for Cosmological Physics, University of Chicago, Chicago, IL 60637, USA*

⁹*Department of Astronomy and Astrophysics, University of California, Santa Cruz, CA 95064, USA*

¹⁰*Boston University Department of Astronomy, 725 Commonwealth Ave, Boston USA*

¹¹*Center for Astrophysics, Harvard & Smithsonian, 60 Garden Street, Cambridge, MA 02138, USA*

¹²*Department of Physics and Astronomy, University of Hawai'i at Mānoa, Honolulu, Hawai'i 96822, USA*

¹³*E.O. Lawrence Berkeley National Laboratory, 1 Cyclotron Rd., Berkeley, CA 94720, USA*

(Received April 4, 2025; Revised May 30, 2025)

Submitted to The Astrophysical Journal

ABSTRACT

We present a simulation of the time-domain catalog for the *Nancy Grace Roman Space Telescope*'s High-Latitude Time-Domain Core Community Survey. This simulation, called the Hourglass simulation, uses the most up-to-date spectral energy distribution models and rate measurements for ten extra-galactic time-domain sources. We simulate these models through the design reference *Roman Space Telescope* survey: four filters per tier, a five day cadence, over two years, a wide tier of 19 deg² and a deep tier of 4.2 deg², with ~20% of those areas also covered with prism observations. We find that a science-independent *Roman* time-domain catalog, assuming a S/N at max of >5, would have approximately 21,000 Type Ia supernovae, 40,000 core-collapse supernovae, around 70 superluminous supernovae, ~35 tidal disruption events, 3 kilonovae, and possibly pair-instability supernovae. In total, Hourglass has over 64,000 transient objects, 11 million photometric observations, and 500,000 spectra. Additionally, Hourglass is a useful data set to train machine learning classification algorithms. We show that SCONE is able to photometrically classify Type Ia supernovae with high precision (~95%) to a $z > 2$. Finally, we present the first realistic simulations of non-Type Ia supernovae spectral-time series data from *Roman*'s prism.

Keywords: Surveys (1671), Catalogs (205), Time domain astronomy (2109), Space telescopes (1547), Astronomical simulations (1857)

Corresponding author: B. M. Rose
Ben.Rose@baylor.edu

* Einstein Fellow

1. INTRODUCTION

The *Nancy Grace Roman Space Telescope* is NASA’s next flagship mission, with a design focused on answering questions in cosmology, measuring exoplanet demographics, and conducting near-infrared astrophysics surveys (Spergel et al. 2015). It has a 2.4 meter primary mirror and will be located at the Earth-Sun L2 point. *Roman*’s primary instrument is the Wide Field Instrument (WFI), which has 18 near-infrared detectors ($0.48\text{--}2.3\ \mu\text{m}$ and $0.11\ \text{arcsec/pix}$) that create a field-of-view of $0.281\ \text{deg}^2$: an expansive $200\times$ the field-of-view of the *Hubble Space Telescope*’s Wide Field Camera 3 infrared channel.¹ NASA has committed to launch the *Roman Space Telescope* no later than May 2027.

Up to 75% of the first five years of *Roman Space Telescope* observations will be dedicated to large core surveys. The data set from the *Roman* High-Latitude Time-Domain Core Community Survey will provide the majority of the extra-galactic transient data from this mission. The observing strategy for this survey is not finalized, however, an initial reference survey has been developed (Rose et al. 2021; Hounsell et al. 2023).² This reference survey is not a fully optimized design, but rather an example to show that the science goals of *Roman* are achievable. It is also an excellent baseline for simulations of ancillary science, such as a generic time domain catalog.

The most recent High-Latitude Time-Domain reference survey (Rose et al. 2021; Hounsell et al. 2023) will observe one or two discrete locations in the *Roman* continuous-viewing-zone—within 36° of either the north or south ecliptic pole—every 5 days over the course of two years. The reference survey includes two filter-depth combinations, referred to as tiers: one tier with $\sim 19\ \text{deg}^2$ of *RZYJ* ($0.48\text{--}1.454\ \mu\text{m}$) at 25.5 mag depth per visit and another $\sim 5\ \text{deg}^2$ field with *YJHF* ($0.927\text{--}2.00\ \mu\text{m}$) at 26.6 mag depth. Additionally, there are slitless spectroscopy observations of about 1/10th the total area (Rose et al. 2021; Rubin et al. 2022; Wang et al. 2023) using an $R \sim 100$ prism ($0.75\text{--}1.80\ \mu\text{m}$).

The reference survey is used to demonstrate that *Roman* can achieve its science goal of understanding dark energy. As such, there is a need to investigate the expected time-domain data set. It is important for the community to understand the capabilities of the *Roman Space Telescope* as NASA starts the public process of

defining the core community surveys³. It is valuable to not only release a simulated data set, but also the simulation input files, as this can be used for studying contaminated cosmological samples, and has been requested by the community⁴.

Simulating a wide range of time-domain sources has previously been done for the Vera C. Rubin Legacy Survey of Space and Time (LSST). Both the Photometric LSST Astronomical Time Series Classification Challenge (PLAsTiCC, The PLAsTiCC team et al. 2018; Kessler et al. 2019) and the Extended LSST Astronomical Time-series Classification Challenge⁵ (ELAsTiCC) have produced large simulated data sets for community analysis. These two programs were designed for improving photometric-classification and data-broker pipelines, respectively.

In this work, we present the Hourglass simulation: a suite of simulated light curves and spectral time series data for ten extragalactic transient types. Hourglass will allow the community to evaluate the science possible with the current *Roman* High-Latitude Time-Domain Core Community survey, and assist in the ability to optimize this survey. In Section 2, we present the assumptions and methods of our simulations. In Section 3, we present results of our simulations. Finally, in Section 4, we discuss what might be possible in future simulations.

2. SIMULATIONS

For this work, we use the simulation components of the SuperNova ANALysis Software (SNANA, Kessler et al. 2009a) with the PIPPIN (Hinton & Brout 2020) pipeline manager. A brief overview of the simulation is as follows:

1. Fluxes are generated from an astronomical source spectral-temporal model that starts from a rest-frame spectral model for each epoch. The model is then subject to astrophysical and observational effects such as redshifting.
2. The source’s spectra are integrated for each filter (or spectral resolution element) to obtain broadband fluxes.
3. Finally, survey and follow up logic is applied.

The details of our simulations are explained in the following sections, first looking at the sources (Section 2.1), then summarizing the survey design, selection criteria

¹ https://roman.gsfc.nasa.gov/science/WFI_technical.html

² During the time of this paper was written, the Core Community Survey Definition Committees met and provided a proposed survey definitions. The *Roman* Time Allocation Committee is currently meeting to finalize the survey.

³ https://roman.gsfc.nasa.gov/science/ccs_community_input.html

⁴ https://pcos.gsfc.nasa.gov/TDAMM/docs/TDAMM_Report.pdf

⁵ https://portal.nersc.gov/cfs/lsst/DESC_TD_PUBLIC/ELASTICC/

and other astrophysical parameters (Section 2.2), and describing the noise and instrument characteristics (Section 2.3).

The full set of simulation input files used can be found at https://github.com/Roman-Supernova-PIT/hourglass_snana_sims and in the data release (<https://doi.org/10.5281/zenodo.14262943>).

2.1. Transients

In total, we simulate ten transient types as our source models. A list of transient types and their associated parameters can be found in Table 1. We take the spectral energy distributions (SED), absolute magnitudes, and rates from various sources in the literature. For our simulations, we predominately use the publicly released models developed for PLAsTiCC⁶ (Kessler et al. 2019; PLAsTiCC Modelers 2022), though we use several models that have been updated since then. We use the SED, luminosity functions, and luminosity scatter models that comes with each model, unless noted otherwise.

We note that our simulations do not use the library of near-infrared-extended SED models developed for the recently published OpenUnivers2024 (OpenUniverse et al. 2025). This is because the diversity of transient types included in the OpenUnivers2024 transients' template library is significantly reduced compared to the PLAsTiCC transient library. Leaving out the near-infrared extensions is only apparent in one or two bands of the lowest redshift objects.

2.1.1. Type Ia Supernovae

For the simulation of Type Ia supernovae (SNe Ia), we use the generative SALT3-NIR model for the SED (Pierel et al. 2022). We use the well-tested intrinsic scatter model presented in Guy et al. (2010) along with the population parameters defined in Kessler & Scolnic (2017). The differences between scatter models (i.e., Guy et al. 2010; Chotard et al. 2011; Popovic et al. 2021a) are negligible (<0.1 mag) when not focusing on precise cosmological distances. SALT3-NIR is defined from 2,800–20,000 Å.

We use the volumetric rate of:

$$R(z) = \begin{cases} 2.4 \times 10^{-5} \times (1+z)^{1.55} \text{ yr}^{-1} \text{ Mpc}^{-3} & \text{if } z < 1.0 \\ 7.5 \times 10^{-5} \times (1+z)^{-0.1} \text{ yr}^{-1} \text{ Mpc}^{-3} & \text{if } z \geq 1.0 \end{cases} \quad (1)$$

as measured in Strolger et al. (2020) thus updating the volumetric rate assumptions used in previous *Roman* simulations (Hounsell et al. 2018; Rose et al. 2021). For

this simulation, we assume that the measured redshift-dependence of the rate from $1 < z < 2$ can be extrapolated out to $z = 3$, as there are no available measurements of SN Ia rates above redshift 2.

For each simulated SN Ia, the host galaxy is assigned following the SN rates as a function of host galaxy properties published by Wiseman et al. (2021), similarly to the method presented in Vincenzi et al. (2021). Host galaxies are selected from the 3DHST program (Van Der Wel et al. 2014). Correlations between SN properties and host galaxy properties are modeled following the approach presented by (Popovic et al. 2021b).

2.1.2. SNIa-91bg Supernovae

SN1991bg-like supernovae (SNIa-91bg) represent the faintest end of the thermonuclear SN Ia population (Filippenko et al. 1992). These objects represent about 15%–20% of the SN Ia class (Li et al. 2011b; Graur et al. 2017). For these simulations, we use a SNIa-91bg model derived in González-Gaitán et al. (2014), which contains 35 templates over a wavelength range of 1,000–12,000 Å.

We simulate SNIa-91bg supernovae at 15% of the rate of SNe Ia (see Equation 1). The high-redshift rate of SNIa-91bg SN is uncertain since they are preferentially found in more passive and massive galaxies (González-Gaitán et al. 2011) and a stronger decline in rate at higher redshift is expected. We keep the rate of SNIa-91bg SNe at 15% of Equation (1), and use the SNIa-91bg-host galaxy correlations assumed in the Dark Energy Survey SN simulations (Vincenzi et al. 2021).

2.1.3. Type Iax Supernovae

Type Iax supernovae (or 02cx-like, Li et al. 2003, hereafter SNe Iax) are thought to be failed thermonuclear runaways (Foley et al. 2013; Jha 2017). For this simulation, we use templates created by S. Jha and M. Dai⁷ that are based on observations of SN 2005hk and are adapted to match the luminosity function and light-curve parameters for SN Iax. The 1000 SN Iax templates have a rest-frame wavelength range of 1,000–25,000 Å and include A_V variations (Vincenzi et al. 2021).

The volumetric rate for SN Iax is set by local measurements relative to the SNe Ia rate (30%, Foley et al. 2013; Miller et al. 2017). With this information, we simulate SN Iax at 30% of the SNIa volumetric rate (see

⁶ <https://zenodo.org/record/6672739>

⁷ <https://github.com/RutgersSN/SNIax-PLAsTiCC>

Table 1. Summary of Transient Input Values

Transient	SED Model	SED Wavelengths (Å)	Simulated Redshifts	Simulated Phase
SN Ia	Pierel et al. (2022) *	2,800–20,000	0.03–2.9	–40–90
SNIa-91bg	González-Gaitán et al. (2014) *	1,000–12,000	0.03–2.9	–40–90
SN Iax	Jha & Dai 2019	1,000–25,000	0.03–2.9	–40–90
CCSN	Vincenzi et al. (2019) *	1,605–11,000	0.03–2.9	–40–90
SLSN-I	MOSFiT slsn	1,000–11,000	0.03–2.9	–50–150
TDE	MOSFiT tde	1,000–11,000	0.03–2.0	–40–90
ILOT	MOSFiT csm	1,100–11,000	0.03–1.0	–20–25
KN	Bulla (2019)	100–99,900	0.03–1.5	–2–20
PISN	MOSFiT default	1,000–11,000	0.03–2.9	–50–150
AGN	ELAsTiCC, in prep.	100–20,000	0.03–2.9	–40–90

*These models have been updated since PLAsTiCC to extend their wavelengths into the rest frame near-infrared.

Equation 1), and use the transient-host galaxy correlations assumed in the Dark Energy Survey SN simulations ([Vincenzi et al. 2024](#)).

2.1.4. Core-collapse Supernovae

For core-collapse supernovae (Type Ib/c and Type II, hereafter referred to as CCSN) we use 65 spectral models from [Vincenzi et al. \(2019\)](#), including the CCSN-host galaxy property correlations. We use the rates derived from the GOODS, CANDELS, and CLASH surveys ([Strolger et al. 2015](#)). This rate is

$$R(z) = 0.015 \frac{(1+z)^5}{((1+z)/1.5)^{6.1} + 1} \text{ yr}^{-1} \text{ Mpc}^{-3} \quad (2)$$

This rate was only measured out to $z \sim 2.5$, therefore we make the assumption that it is valid to $z = 3$. Additionally, each parameter in this equation has an uncertainty of $\sim 10\%$.

2.1.5. Superluminous Supernovae

Superluminous supernovae type I (SLSN-I) are some of the most luminous transients, with a peak absolute magnitude of $\lesssim -21$ mag. They are fairly rare and only recently discovered ([Quimby et al. 2011](#); [Chomiuk et al. 2011](#)). For this simulation, we use the Modular Open-Source Fitter for Transients (**MOSFiT**, [Guillochon et al. 2018](#)) generated spectral-temporal SEDs using the **MOSFiT slsn** model that assumes a magnetar engine and a blackbody SED ([Kasen & Bildsten 2010](#); [Nicholl et al. 2017](#)). This model is defined from 1,000–11,000 Å and resulted in 960 templates.

We use the SLSN rate from [Prajs et al. \(2017\)](#):

$$R(z) = 2.0 \times 10^{-8} \times R_{\text{MD14}}(z) \quad (3)$$

where $R_{\text{MD14}}(z)$ is the redshift dependent component of the cosmic star formation rate defined in [Madau & Dickinson \(2014\)](#) and repeated here:

$$R_{\text{MD14}}(z) = \frac{(1+z)^{2.7}}{((1+z)/2.9)^{5.6} + 1} \text{ yr}^{-1} \text{ Mpc}^{-3} \quad (4)$$

This rate is a slight variation to what was reported in [Madau & Dickinson \(2014\)](#). We do not use the multiplicative scaling of 0.015 that is seen in Equation 15 of [Madau & Dickinson \(2014\)](#) since we want to normalize each astrophysical object to its own $z = 0$ rate. This SLSNe rate is within the current uncertainty presented in the literature ([Quimby et al. 2013](#); [McCrum et al. 2015](#); [Prajs et al. 2017](#)), and reflects the fact that the SLSNe rate appears to follow the cosmic star formation rate ([Prajs et al. 2017](#)). For the SLSN, we use the transient-host galaxy correlations derived for the OpenUniverse2024 simulations ([OpenUniverse et al. 2025](#)). These are built off of the work of the Simulated Catalog of Optical Transients and Correlated Hosts (SCOTCH, [Lokken et al. 2023](#)), but extended into the *Roman* wavelength range.

2.1.6. Tidal Disruption Events

Tidal disruption events (TDEs) occur when stellar objects are tidally ripped apart as they fall into a black hole. Typically, this takes place near supermassive black holes due to the required orbital-to-stellar radius ratio ([Rees 1988](#); [Mockler et al. 2019](#)). We use SEDs generated from the **MOSFiT tde** model and transient-host galaxy property correlations derived for the OpenUniverse2024 and SCOTCH simulations ([OpenUniverse et al. 2025](#); [Lokken et al. 2023](#), respectively).

We use the TDE rate from Kochanek (2016) and van Velzen (2018):

$$R(z) = 10^{-6} \times 10^{-5z/6} \text{ yr}^{-1} \text{ Mpc}^{-3} \quad (5)$$

We assume this rate holds throughout cosmic time, however, Kochanek (2016) argues that the rate of TDE’s sharply drops off at $z = 1$. This claim is something *Roman Space Telescope* can test.

2.1.7. Intermediate Luminosity Optical Transients

Intermediate luminosity optical transients (ILOTs) have peak luminosities between classical novae and supernovae and display signs of interaction with a dense circumstellar material, similar to SNe IIn. The 385 templates we use were generated using the MOSFiT csm model following parameter ranges described in Villar et al. (2017) and Chatzopoulos et al. (2012) with a rest-frame wavelength range of 1,000–11,000 Å. We assume a volumetric rate that is 6% that of the CCSN rate defined in Equation (2), and use the CCSN-host galaxy correlations from the Dark Energy Survey. This rate is from Li et al. (2011a) following the assumption that ILOTs have a similar progenitor as Type IIn supernovae.

2.1.8. Kilonovae

Kilonovae (KN) are the merger of two compact objects, typically neutron stars (Kasen et al. 2017). We use the SED model defined in Bulla (2019). Our model has 550 templates with a rest-frame wavelength range of 100–99,900 Å. We use the volumetric rate of

$$R(z) = 3.2 \times 10^{-7} \text{ yr}^{-1} \text{ Mpc}^{-3} \quad (6)$$

from a recent estimate of the binary neutron stars (Abbott et al. 2021). However, this rate is very uncertain, and the total number of KN observed by *Roman Space Telescope* could be over or underestimated by a factor of ~ 3 (Abbott et al. 2021). Additionally, to reduce Poisson noise in the detection rate, we scale up these simulations by using a rate five times that of Equation (6) to ensure the total detected objects is > 10 .

2.1.9. Pair Instability Supernovae

Pair instability supernovae (PISN) are proposed to arise when low-metallicity Population III stars, with $M_{\star} \sim 140\text{--}260 M_{\odot}$, reach sufficiently high core temperatures that γ -rays produce electron-positron pairs (Barkat et al. 1967; Kasen et al. 2011). PISN are extremely high redshift transients, and therefore only a few possible PISN have been reported (Gal-Yam & Leonard 2009; Cooke et al. 2012; Kozyreva et al. 2018; Gomez et al. 2019; Schulze et al. 2024; Aamer et al. 2024). We use the MOSFiT default model with PISN parameters

as described in Villar et al. (2017). We use 1000 SED time series templates that have a rest-frame wavelength range of 1000–11000 Å.

A volumetric rate for PISN presented stated in Briel et al. (2022). We fit a polynomial to the data presented and obtain a volumetric rate of

$$R_{B22}(z) = [-4.08 + 30.56z - 19.91z^2 + 16.82z^3 - 3.00z^4] \text{ yr}^{-1} \text{ Gpc}^{-3} \quad (7)$$

At $z = 1$ it is nearly twice the PISN rate (Pan et al. 2012) used in previous simulation efforts. Since PISN are from extremely massive stars, we use the CCSN-host galaxy correlations derived from the Dark Energy Survey.

2.1.10. Active Galactic Nuclei

We simulate 500 active galactic nuclei (AGN) that have a constant volumetric rate ($1.0^{-3} \text{ Mpc}^{-3}$) for the redshift range $0.03 < z < 3$. We use the analytical model that has been generated for the ELAsTiCc simulations. It is a damped random walk model that includes the possibility of changing look behavior. The simulation varies the black hole mass, Eddington ratio (Weigel et al. 2017; Sartori et al. 2019), and i -band absolute magnitude (Shen 2013) for each object. This model will be described in further detail in the ELAsTiCc paper in prep.

2.1.11. Non-Variable Sources

To allow for the widest range of tests, we include “fixed magnitude sources.” These are objects that have the same magnitude at all epochs, but a different random magnitude is chosen for each event. We simulate 1000 events that range in apparent magnitude from 18 to 30 mag.

2.2. Survey Design and Detection

We follow the “25% spectroscopic time” survey strategy laid out in Rose et al. (2021), where the wide tier is observed with the F062, F087, F106, and F129 (colloquially R , Z , Y , J) and covers 19.04 deg^2 . The deep tier is observed in F106, F129, F158, and F184 (Y , J , H , F) and covers 4.20 deg^2 . These exposure times and areas were determined when the average slew and settle time would have been ~ 70 s. This has since been reduced, and the expectation is that the actual survey should have more “open-shutter” time. For these simulations, we keep the 70 s slew and settle time assumption. With many of the SED models only extending redward to 11,000 Å, the simulations for these events only have R , Z , and Y until $z > 0.175$ where there is full coverage of the J -band. We locate the two tiers such that

Table 2. Summary of Observing Strategy from Rose et al. (2021)

Filters	Exp. Time (s)	No. of Pointings	Area (deg ²)
<i>Wide Tier</i>			
RZYJ	160;100;100;100	68	19.04
prism	900	12	3.36
<i>Deep Tier</i>			
YJHF	300;300;300;900	15	4.20
prism	3600	4	1.12

they do not overlap and are located near Euclid’s Deep Field South, roughly (RA, dec) = (04:04:58, −48:25:23). We also simulate the slitless prism with 12 wide-tier and 4 deep-tier pointings (3.36 and 1.12 deg² respectively). All exposure times and numbers of pointings per tier are taken from Rose et al. (2021) and summarized in Table 2. We have designed these simulations so that they can be updated once an observational strategy has been selected by the *Roman* scientific community.

The Roman Time Allocation Committee (ROTAC) recently released recommendations for the Core Community Surveys (Observations Time Allocation Committee & Community Survey Definition Committees 2025). This is similar to the design reference mission but increases the area of the deep tier (from 15 to 23 pointing) and adds additional filters at the cost of using an interweaving cadence (rotating sets of filters so an observation is still taken every 5 days but the filter to same filter cadence is 10 days). As a result, the expected number of objects increases by approximately 25–30%. Additionally, they recommended a pilot and extended surveys outside the core, two-year, survey. We plan on updating these simulations when the a stable version of the ROTAC recommendations are implemented, likely Fall 2025.

Additionally, these simulations do not account for dithering, roll angles or field edge effects. Some ramifications of these effects have been discussed previously in Rose et al. (2021) and Hounsell et al. (2023). For current approximations of these effects, one can discard one of every eight photometric observations, representing *Roman Space Telescope*’s $\sim 7/8$ ths focal plane fill factor.

Regarding detection, we impose a threshold of two observations with $S/N > 5$.⁸ This is a loose quality cut that only removes the lowest signal to noise simulated events. It is also a fairly standard cut applied to real data in order to remove subtraction artifacts (which are not included in our simulations). This approach of only applying a loose cut in our simulations will allow users to implement their own quality cuts. We do not apply any selection effects from spectroscopic follow-up.

We use host-galaxy characteristics from the 3DHST program (Van Der Wel et al. 2014). Our sample contains 110,798 entries with galaxy properties derived from real data⁹. This set of host galaxies were used in the pixel simulations found in Wang et al. (2023). However, this choice limits our simulations to a redshift maximum of 3. This upper limit doesn’t affect the majority of transients included in the simulations, except for SLSNe and PISN, which in principle could be detected far beyond this redshift with *Roman*. In the future, we plan to update the host galaxy catalogs used for our simulations using N-body simulations such as the Deep Realistic Extragalactic Model (DREaM) Galaxy Catalog (Drakos et al. 2022).

For host galaxy dust, we use an exponential plus gaussian “galactic line-of-sight” model for A_V presented in Wood-Vasey et al. (2007, Equation 2). The Gaussian core has a standard deviation of $\sigma = 0.6$ mag and the exponential tail has a rate parameter $\tau = 1.7$ mag. These values are taken from Vincenzi et al. (2021). For R_V , we simulate a range of values, 3.0–3.2, peaking at 3.1. For SN Ia, the host-galaxy dust is already a part of the SALT2 and population models, therefore we don’t include more.

We use the Milky Way color law from Fitzpatrick (1999) assuming an $R_V = 3.1$ and a dust map from Schlafly & Finkbeiner (2011). In this simulation, we assume a flat- Λ CDM cosmology with $\Omega_M = 0.3$ and $h = 0.7$.

2.3. Roman WFI Characteristics

The latest hardware characteristics for the *Roman Space Telescope*’s WFI can be found at <https://roman.gsfc.nasa.gov/science/WFItechnical.html>. This URL contains the current estimates for the filter transmission, detector efficiency, prism two-pixel dispersion, and filter throughput. These parameters are incorporated

⁸ This cut is on single epoch images. Presumably one can stack epochs and increase the total detections for slow transients, such as PISN and SLSN.

⁹ <https://github.com/srodneym/romansims/blob/main/romansims/catalogs.py>

into the simulation’s noise model by the creation of appropriate definitions of filter and prism zero-points and point-spread functions. Figure 1 (*left*) shows the filter transmission functions used and Figure 1 (*right*) shows the prism’s wavelength dependent two-pixel dispersion.

For the SNANA simulations, the noise values (thermal, sky, and read noises) are calculated to include exposure times. Thus, we have different noise and zero-points per filter and per tier. Our values are presented in Table 3 and are updated from those assumed in the simulations presented by Hounsell et al. (2018). Since these simulations are based on the current reference survey design (Rose et al. 2021), we use the same exposure times (see Table 2) and average slew and settle time (70 s). However, other instrument properties have been updated since then. The are available in Mosby et al. (2020) or on the WFI technical specifications website, https://roman.gsfc.nasa.gov/science/WFI_technical.html. WFI underwent thermal-vacuum testing in the first half of 2024. We have set up our simulations such that we can update them with post-thermal-vacuum values when they become available.

2.3.1. Point Spread Function

We take the point spread function (PSF) from the *Roman* WFI technical website mentioned above. The PSF has a large variation across the field of view, therefore, we use the median of the best and worst noise equivalent areas (NEA). The values are presented in Table 3. Though we only have one area per filter, we account for the significant NEA change across the field-of-view through the variation of the zero point. This does not fully match the effects of a changing PSF (e.g., it has no dependence on source color), but it does approximate the changes in signal to noise as a point source gets spread over different areas.

2.3.2. Zero-point Values

The simulations use an exposure time-dependent zero-point defined as:

$$ZP_{\text{AVG}} = ZP + 2.5 \log_{10}(t) \quad (8)$$

with ZP being the magnitude that results in one count per second and t being the total exposure time. ZP was calculated by using the filter effective area curves provided available at the WFI technical specifications website and integrating an flat-AB spectrum. There is a significant scatter in zero-point and PSF across the field of view. To approximate these effects, we include a zero-point scatter with a standard deviation of 0.15 mag.

This is a stochastic effect that depends on where a source lands on the field of view.

2.3.3. Read Noise

The simulation uses the read noise as a function of exposure time. Since near-infrared detectors use non-destructive reads, and *Roman* will not download every resultant that is read (Casertano 2022; Gomez 2023), the total read noise as a function of exposure time can be defined as

$$\sigma_{\text{read}} = \sqrt{\sigma_{\text{floor}}^2 + \sigma^2 \frac{(n-1)}{n(n+1)}} \quad (9)$$

where $n = t_{\text{exp}}/3.04$ s or number of reads for a given exposure (t_{exp}). We use $\sigma_{\text{floor}}^2 = 25$ and $\sigma^2 = 12 * 16^2 = 3072$ as defined by measurements reported by the project in 2021.¹⁰ These values are given from the project on the WFI technical specifications website. This is the same equation for read noise as used in Hounsell et al. (2018), but the final numbers are reduced slightly. The final read noise per filter for our given exposure times can be seen in Table 3.

2.3.4. Sky Noise

The simulation combines all sky noise together—zodiacal, and thermal—for a given exposure length. The sky-noise is reported as a standard deviation in ADU per pixel. This can be calculated with the following equation:

$$\sigma_{\text{sky}} = \sqrt{t_{\text{exp}}(\sigma_{\text{zodi}}^2 + \sigma_{\text{thermal}}^2)} \quad (10)$$

where t is exposure time, and σ_{zodi} , and σ_{thermal} are given by the project. The dark current is sufficiently small to be ignored this simulation. These values have reduced since Hounsell et al. (2018).

3. LIGHT CURVES AND SPECTRAL TIME SERIES

We provide a summary of the Hourglass simulation in Table 4. We give the median redshift for each type and find it varies as expected depending on the intrinsic magnitude. We show redshift histograms for the different types of transients in Figure 2. Along with this paper, we release the photometry, spectroscopy, and object characterization data as parquet files at <https://doi.org/10.5281/zenodo.14262943>. Details on this data release are described in Appendix A.

We find that SNe Ia, PISN and SLSN can be discovered up to the redshift limit of our simulations at

¹⁰ https://roman.gsfc.nasa.gov/science/RRR/Roman_WFI_Reference_Information_20210125.pdf

Table 3. Roman WFI Characteristics Used in Simulation

Filters	PSF _{NEA} (pix)	σ_{read} (e ⁻ /pix)	$\sigma_{\text{thermal}}^2$ (e ⁻ /s/pix)	σ_{zodi}^2 (e ⁻ /s/pix)	σ_{sky} (ADU/pix)	ZP _{AVG} (mag)
<i>Wide Tier</i>						
R	5.575	9.011	0.003	0.315	7.133	32.129
Z	6.695	10.624	0.003	0.316	5.648	31.303
Y	7.895	10.624	0.003	0.357	6.000	31.356
J	9.210	10.624	0.003	0.359	6.017	31.354
<i>Deep Tier</i>						
Y	7.895	7.450	0.003	0.357	10.392	32.549
J	9.210	7.450	0.003	0.359	10.421	32.547
H	11.140	7.450	0.048	0.339	10.775	32.570
F	16.335	5.942	0.155	0.194	17.723	33.299

NOTE— N_{read} , N_{sky} , and ZP_{AVG} assume the exposure times listed in Table 2.

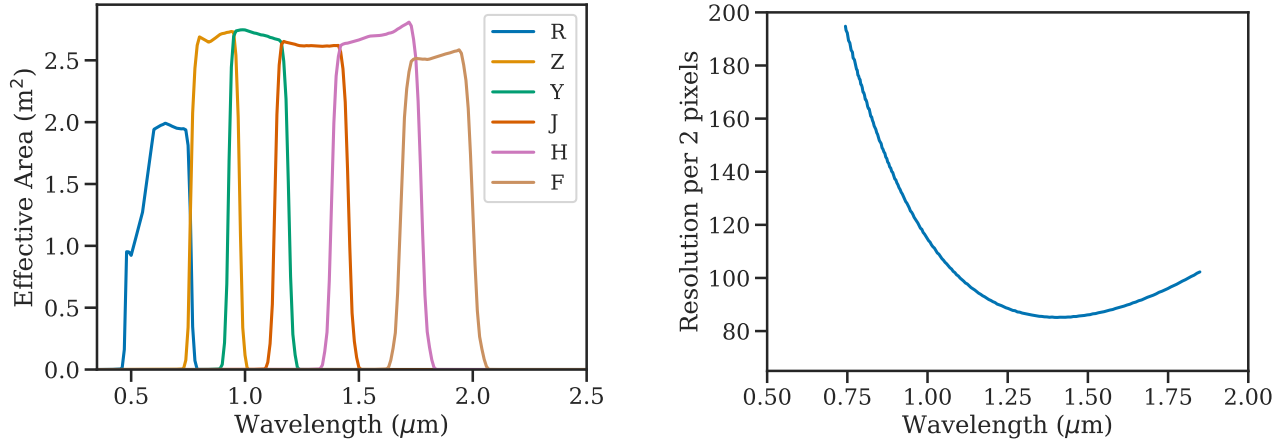


Figure 1. (*left*) The filter transmission and detector response functions used for these simulations. Curves are taken from the Roman project technical resources. (*right*) The prism’s resolution (per 2 pixels) as a function of wavelength. The prism is transmissive from 7,500–18,000 Å. The minimum two-pixel dispersion is ~ 80 around 14,000 Å. Except for the blue edge, most of the wavelengths have an $R \leq 100$.

$z = 3$. In particular, significantly higher redshift PISN and SLSN will be visible, but this simulation artificially cuts off at $z = 3$. Moriya et al. (2022) estimated around 100 PISN at $z > 5$ and about a dozen SLSN at the same redshift range. Due to our redshift range, our simulations are not directly comparable but these values are not inconsistent since Hourglass is only seeing the “low- z ” tail of the PISN and SLSN distributions.

For each class of transient we see the expected dropoff in number due to selection effects (Figure 2). This effect is most obvious in SNe Ia and CCSNe. Additionally, we agree with Inayoshi et al. (2024) that *Roman* will

observe 10–60 TDEs, though our number suggests the higher side of that range.

To better understand the redshift histograms, we show the peak AB-magnitude in Y-band of each object type versus redshift in Figure 3. The precision of SNe Ia as standard candles is immediately obvious, as they have the tightest scatter in magnitude versus redshift space. We can also see that the magnitude limits are around 28th mag.

To demonstrate the detection limits per tier, we show the relation between S/N and peak magnitude in Figure 4. We find detection limits of S/N of 5 for magnitudes of $\sim 27.5^{\text{th}}$ mag and $\sim 26.5^{\text{th}}$ mag for Y and J

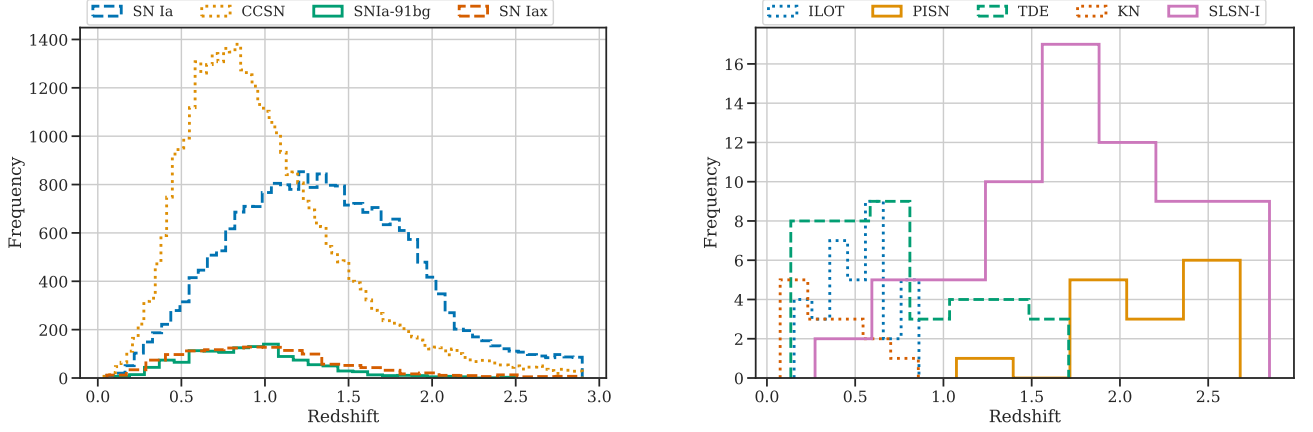


Figure 2. Redshift distribution of recovered transients. The (*left*) panel shows the redshift distributions for high-volume transients such as CCSNe and SNe Ia, as well as for the fainter SN-Ia-like objects (SNe Iax and SNIa-91bg). The (*right*) panel shows the redshift distribution of rarer transient events, including SLSNe, TDEs, ILOTs, KNe, and PISNe. These distributions are more uncertain due to the limited data used in rate models, particularly at redshifts that will be probed by *Roman*. We do not present the redshift distributions for the AGN in this figure since we generated a fixed number of events rather than use a redshift dependent volumetric rate. The light curves and spectra are still in the data release.

Table 4. Hourglass Catalog Summary

Transient	Total Detected Detected	Median S/N at Maximum	Median Redshift
SN Ia	21,700	13.5	1.32
SNIa-91bg	1,300	10.6	0.84
SN Iax	1,300	8.5	0.95
CCSN	39,000	8.8	0.90
SLSN-I	70 ^a	32.4	1.82
TDE	39	13.5	0.65
ILOT	35	6.7	0.49
KN ^b	14	7.9	0.35
PISN	15 ^a	8.2	2.23
AGN	139	13.6	1.78

NOTE— Detected values are rounded according to the expected counting statistics uncertainty. The ROTAC recommend survey should increase these numbers by 25–30% for the core survey. Including the pilot and extended surveys, we expect over 100,000 transients.

^aOne could use multi epoch stacked images and increase the total detections for slow transients.

^bThis simulated KN rate is five times that of [Abbott et al. \(2021\)](#) to overcome Poisson noise, which has stated uncertainty up to a factor of four.

All of these results are highly dependent on the assumed rates. For the most rare transients, such as PISN and KN, the rates can have an uncertainty range of a factor of 2 or 3 ([Briel et al. \(2022\)](#); [Pan et al. \(2012\)](#) and [Abbott et al. \(2021\)](#), respectively). Additionally, rates are poorly defined at the higher redshifts. For example, the SN Ia rates have only been measured to $z \sim 2$ and above $z > 1$ the uncertainty is significant ([Strolger et al. 2020](#)). Yet for this work, we assume these rates are valid to $z = 3$. *Roman Space Telescope*’s field of view, survey length, and depth will allow it to probe parameter space that has never previously been explored. Though there are high-redshift transients discovered with JWST, (e.g., [Pierel et al. 2024, 2025](#); [DeCoursey et al. 2025](#)), these are not sufficiently large enough samples to improve our rate estimates.

We showcase example light curves of the median S/N at max for each time-domain class in Figure 5. The 5-day observer frame cadence will allow for very high sampling, particularly for the longer lasting transients like SLSNe, TDEs, and PISNe. For KNe, this cadence is closer to the decay rate of the explosions and thus limits their detectability.

3.1. Comparison with Current Samples

For SNe Ia, *Roman Space Telescope* will provide an order of magnitude more and reach a redshift of more than twice that of previous cosmological data sets (e.g., [Scolnic et al. 2021](#); [Rubin et al. 2023](#); [Sánchez et al. 2024](#)). In Figure 6 we compare the redshift distribution of the *Roman* SN Ia sample with the Dark Energy Survey Year

for deep and shallow respectively. We are therefore able to translate the relation seen in Figure 3 to the redshift limits in Table 4.

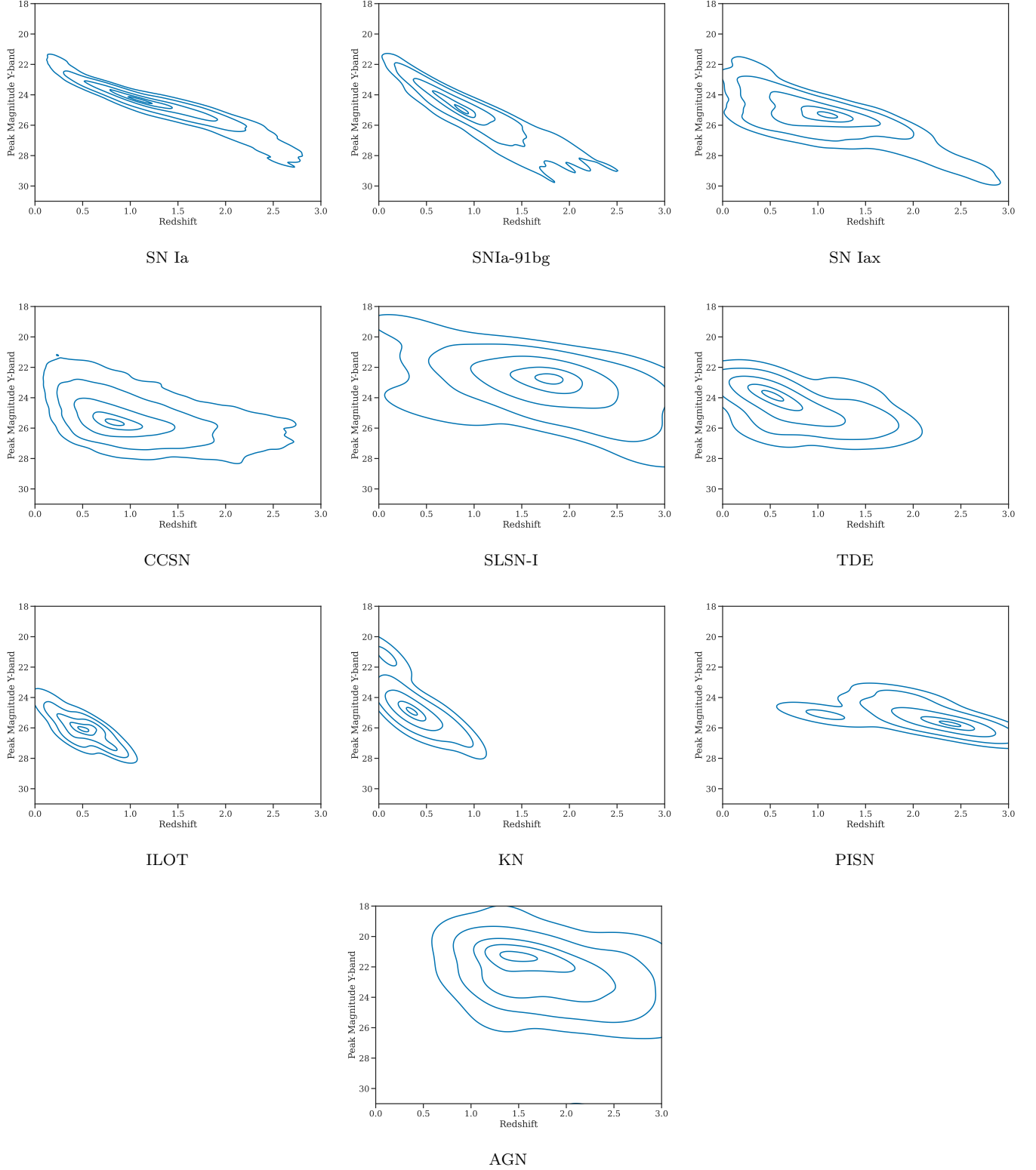


Figure 3. Peak AB-magnitude (in *Roman* Y-band) versus redshift for all ten time-domain classes. Contours are at 2.75, 15.87, 50, 84.13, and 97.25 percentiles. The standard-candle nature of SN Ia can be seen in the first figure. Additionally, the extreme brightness of SLSN-I is visible in the middle frame. From this plot, it is clear that SLSN-I will be visible at redshifts of $z > 3$. There is an artificial cut off at $z = 0.08$ for models with a red-edge of 11,000 Å since they will not have a defined Y-band magnitude.

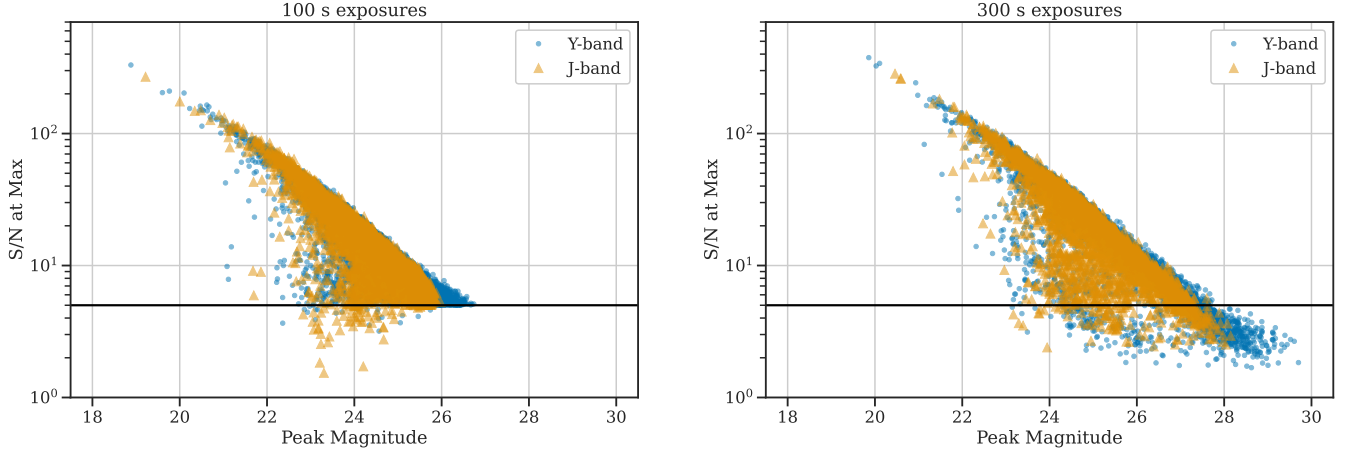


Figure 4. S/N vs. AB-magnitude at peak luminosity for SNe Ia in both Y- and J-bands. $S/N = 5$ is marked with a horizontal line. The *left* panel shows values taken from the wide tier where Y- and J-band each have 100 s exposures. The *right* panel shows data taken from the deep tier where each band has 300 s exposures. With this exposure time, we calculate a $S/N \approx 20$ for a SN Ia of peak magnitude ~ 25 mag.

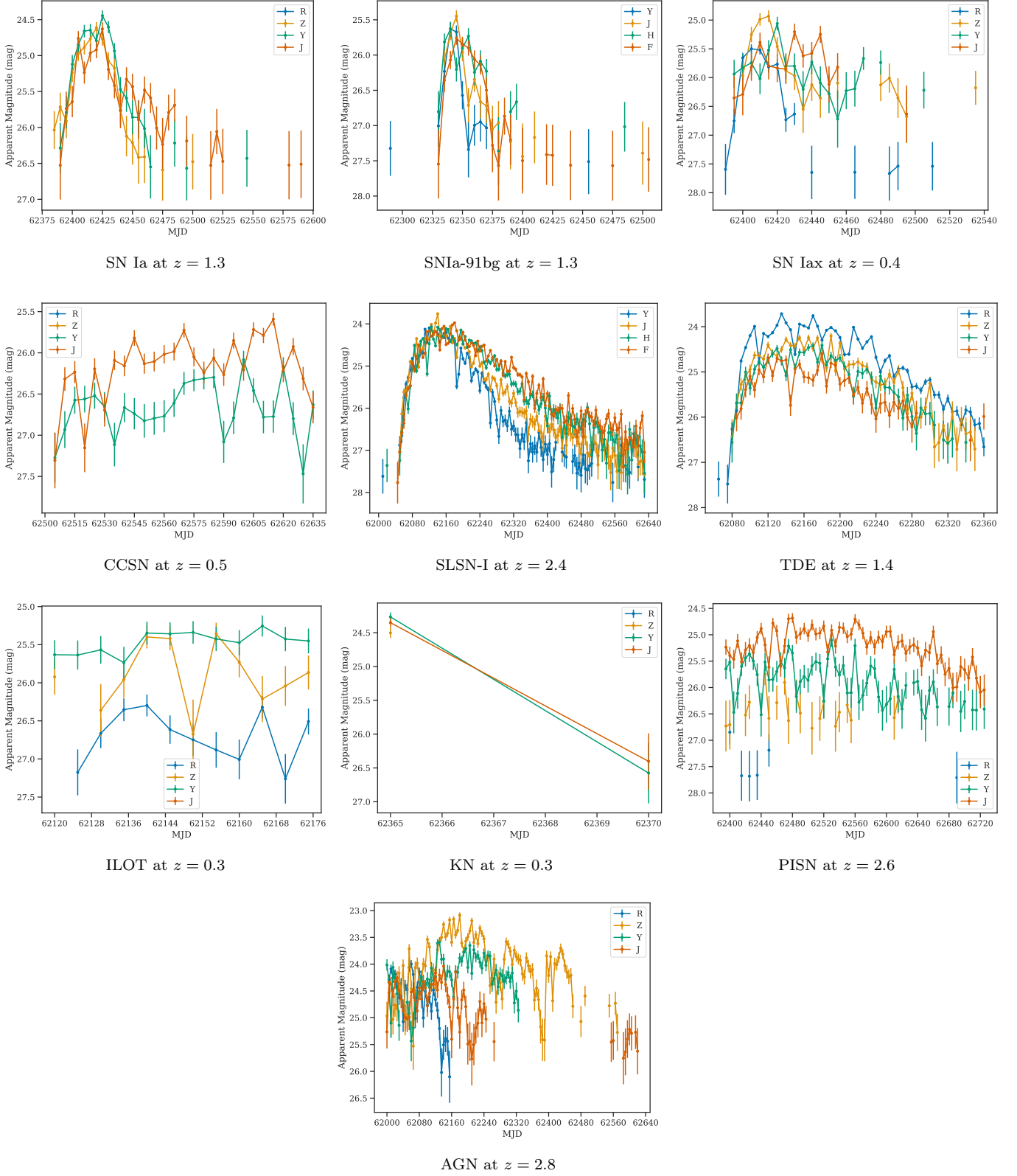


Figure 5. Light curves of the median S/N events per type. The long-lived transients, SLSNe and PISNe, have very well sampled light curves. Fast transients are also well sampled, however, the KN detections have measurements around peak, but very little light-curve information. We needed to go to the 75% percentile S/N at peak in order to get an observation at a second epoch.

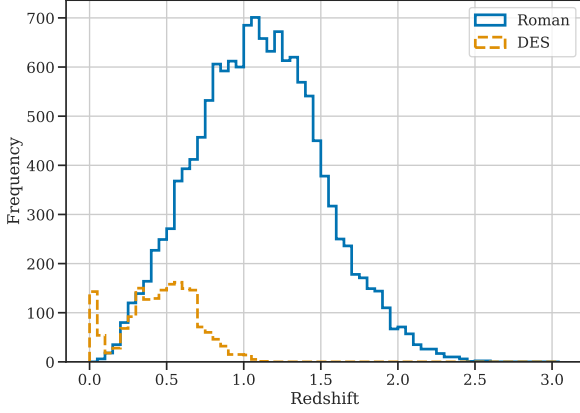


Figure 6. The *Roman* SN Ia sample compared to the recent cosmology sample of the Dark Energy Survey. DES has over 1,500 supernovae in its cosmological sample with very few at $z > 1$. However, we expect *Roman* to have nearly 19,000 SN Ia with the majority above $z > 1$. For this paper, we define “cosmologically useful” as having a S/N at max of greater than 10. This is an overly simple assumption, but still reasonable.

5 data release (DES, [Sánchez et al. 2024](#)). This is the most recent, photometrically classified sample, and represents the current state of the art for Supernova cosmology. However, their sample of approximately 1,500 SN Ia has very few objects above $z > 1$. Comparably, *Roman* is expecting a cosmological sample of over 10,000 SN Ia. In this simulation, we do not perform a full cosmological analysis so we use a S/N at max of greater than 10 as a proxy for “cosmological useful”. With this definition, we have over 19,000 Type Ia supernovae with the majority being above a redshift of one.

3.2. Spectra

In addition to the photometry, we simulate the prism spectral time series for all ten time-domain classes. As an example, we present one SN Ia as observed with the wide-tier exposures, 900 s, in Figure 7. We show 8 phases, from phase -6 to 28 days. Additional late time spectra will be observed with *Roman*, but our SN Ia model stops at a phase of 40 days.

3.3. Photometric Classification of Type Ia Supernovae

For a first test on these simulations, we train and test the binary classification of SCONE ([Qu et al. 2021](#)). SCONE is a convolutional neural network that was used in the DES SN cosmological analysis. For training we use a unique set of only 8,600 SNIa and 8,600 “contamination” objects (CCSN, SN Iax, SNIa-91bg). This simulation uses the same properties as the main Hourglass simulations. The resulting SCONE model can be

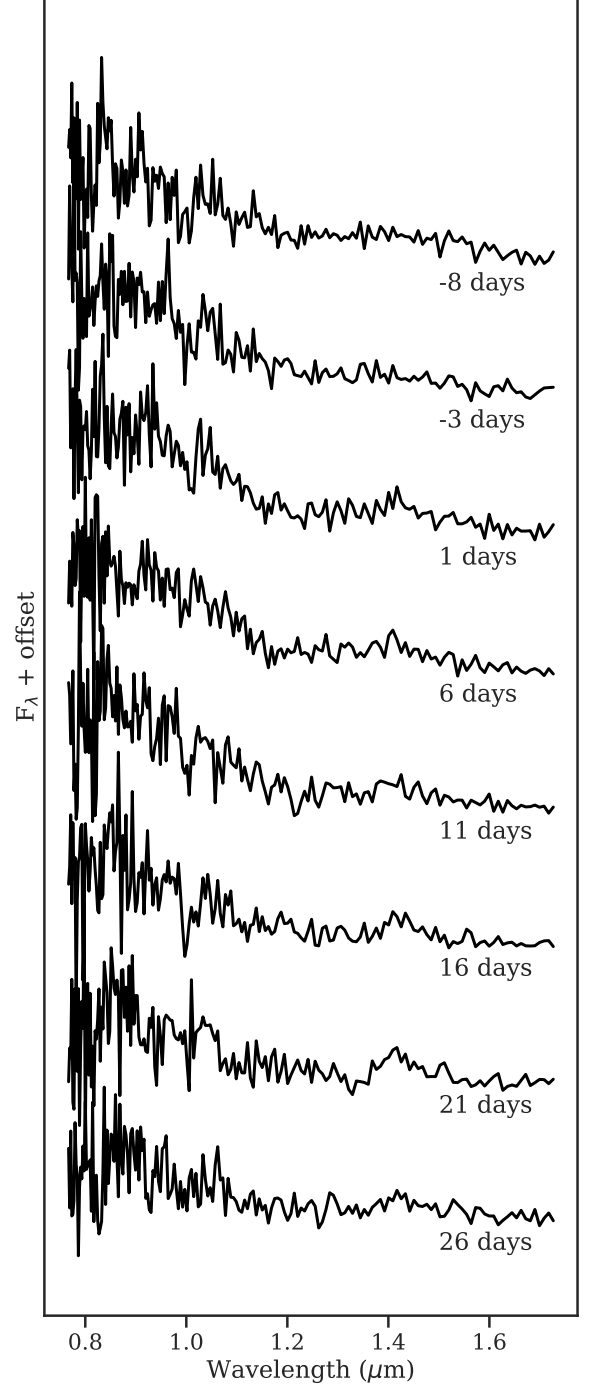


Figure 7. A spectral time series from the *Roman* WFI Prism, presented in the observer’s frame. This is a $z = 0.636$ SN Ia observed in the wide tier (900 s exposures). This results in 9 observations from phase -8 to 26 days.

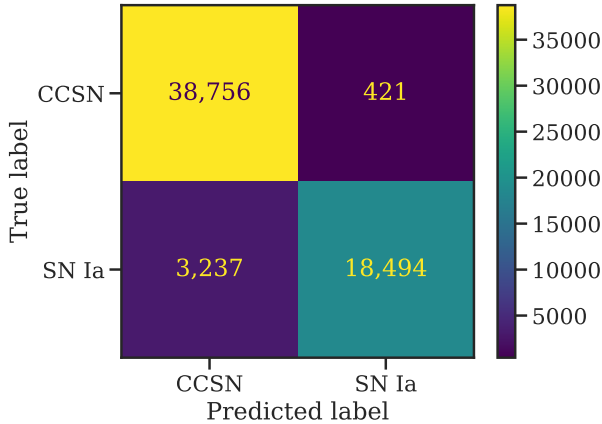


Figure 8. Confusion matrix for the photometric classifier SCONE. We train the binary classification to distinguish between cosmologically useful SNe Ia and contaminants. Contaminates are labeled as CCSN but also contains SNIa-91bg and SN Iax objects. SCONE gets a high recall (85%, i.e. incorrectly classifying a small fraction of the SNe Ia). More importantly, we obtain a high precision (98%), meaning that the predicted SNe Ia label has a low level of contamination.

found at https://github.com/Roman-Supernova-PIT/hourglass_snana_sims/tree/main/3_clas/models/scone.

SCONE requires more than just a single detection, therefore, we add a requirement that there are minimum 5 epochs per transient. This results in 21,731 SNe Ia and 39,177 combined CCSNe, SN Iax, and SNIa-91bg objects. The confusion matrix can be seen in Figure 8. We obtain an accuracy of 94% (number of correct predictions over all predictions), along with a precision of 98% (correctly classified SN Ia over everything classified as a SN Ia) and a recall of 85% (correctly classified SN Ia over everything that is a SN Ia).

We investigate SCONE’s performance as a function of redshift. We present SCONE’s precision, the fraction of correctly labeled SNe Ia over of all events labeled SNe Ia, as a function of redshift in Figure 9. SCONE predominately performs at >95% but has a significant drop off at high redshifts ($z > 2.5$).

4. CONCLUSIONS

In this work, we present and release the Hourglass simulation, a catalog for the *Nancy Grace Roman Space Telescope* High-Latitude Time-Domain Core Community Survey. This simulation includes ten extra-galactic time-domain classes. We run this through the current baseline *Roman* survey: four filters per tier, a five day cadence, a wide tier of 19 deg^2 , and a deep tier of 4.2 deg^2 , with about $\sim 20\%$ of the area also covered by prism observations.

With a detection threshold of $S/N > 5$ in two filters, we find that a *Roman* time-domain catalog would have

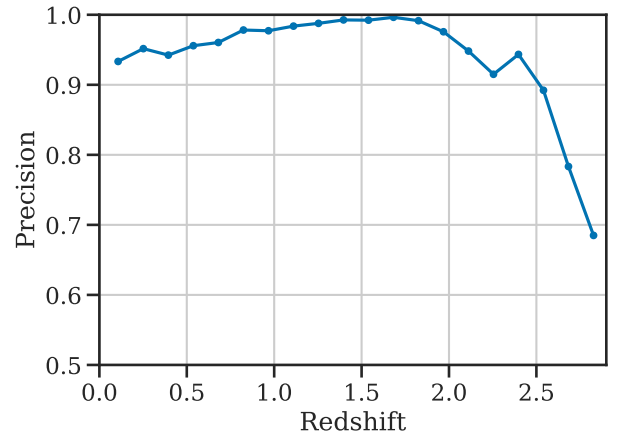


Figure 9. SCONE’s precision is around 99% and peaks near a redshift of 1.7. However, it has a significant drop off at high redshifts. The slightly worse performance at low- z is unexpected. We are unsure if this is a issue with low statistics or the fact that the rest-frame near-infrared features of the transients are different.

approximately 21,700 SNe Ia and 39,000 CCSNe. There would also be around 70 SLSN, 40 TDEs, over 10 PISNe, and possibly 3 KN. We demonstrate that the data set is not purely low S/N observations: most transient classes have a median S/N at maximum luminosity of ~ 10 , and long-lived events have individual light curves with 200 to 500 observations. Additionally, we present the first examples of the expected spectral-time series data from *Roman*’s prism and the SCONE photometric classifier on *Roman* data. The simulated data can be found at <https://doi.org/10.5281/zenodo.14262943>.

Though this simulation surpasses what has come before—in terms of breadth of transient types and the inclusion of the spectral time series data—it is still insufficient for the community’s preparation for the *Roman Space Telescope*. Future simulations need to take into account the hardware knowledge gained from thermal-vacuum testing, test observation strategy recommended by the ROTAC, and continue to add time domain sources such as variable stars. Currently, we don’t expect these changes to have a significant effect on what the *Roman* High-Latitude Time-Domain Core Community Survey catalog looks like, other than increasing the number of transients detected, but we have set up the Hourglass simulation in such a way that we can update it when new input parameters are available.

The authors thank Qifeng Cheng and Konstantin Malanchev for access to the AGN model used in ELAs-TiCc.

Funding for the *Roman* Supernova Project Infrastructure Team has been provided by NASA under contract to 80NSSC24M0023. This work was completed, in part, with resources provided by the University of Chicago’s Research Computing Center. M.V. was partly supported by NASA through the NASA Hubble Fellowship grant HST-HF2-51546.001-A awarded by the Space Telescope Science Institute, which is operated by the Association of Universities for Research in Astronomy, Incorporated, under NASA contract NAS5-26555. Work by R.H. and this material is based upon work supported by NASA under award number 80GSFC24M0006. D.S. is supported by DOE grant DE-SC0010007, DE-SC0021962, the David and Lucile Packard Foundation, and the John Templeton Foundation. R.K. is supported by DOE grant DE-SC0009924.

B.R. lead the project, ran the sims and wrote the first draft of the paper. M.V. assisted in running and analyzing the non-SN Ia the simulations. R.H. provided guidance and help in ensuring the *Roman* specific components were accurately simulated and provided details from the first set of *Roman* simulations using SNANA. H.Q. supported the development and use of the photometric classifier SCONE. L.A. helped validate the data release files. D.S. advised and worked on figures. R.K. supported the development and debugging of SNANA. P.M. helped get the project started with insight from previous *Roman* simulations using SNANA. D.B. provided a technical review of the paper. All authors provided editing and discussions around the paper and the data release.

Software: Matplotlib (Hunter 2007), Numpy (Harris et al. 2020), Pandas (McKinney 2010), PIPPIN (Hinton & Brout 2020), Python, SciPy (Jones et al. 2001), SCONE (Qu et al. 2021), Seaborn (Waskom et al. 2020), SNANA (Kessler et al. 2009b; Kessler & Scolnic 2017).

REFERENCES

- Aamer, A., Nicholl, M., Jerkstrand, A., et al. 2024, 527, 11970
- Abbott, R., Abbott, T. D., Abraham, S., et al. 2021, 913, L7
- Barkat, Z., Rakavy, G., & Sack, N. 1967, 18, 379
- Briel, M. M., Eldridge, J. J., Stanway, E. R., Stevance, H. F., & Chrimes, A. A. 2022, 514, 1315
- Bulla, M. 2019, 489, 5037
- Casertano, S. 2022, Determining the Best-Fitting Slope and Its Uncertainty for up-the-Ramp Sampled Images with Unevenly Distributed Resultants, Nancy Grace Roman Space Telescope Technical Reports, 38 pp.
- Chatzopoulos, E., Wheeler, J. C., & Vinko, J. 2012, 746, 121
- Chomiuk, L., Chornock, R., Soderberg, A. M., et al. 2011, 743, 114

- Chotard, N., Gangler, E., Aldering, G., et al. 2011, *A&A*, 529, L4, <http://www.aanda.org/10.1051/0004-6361/201116723>
- Cooke, J., Sullivan, M., Gal-Yam, A., et al. 2012, 491, 228
- DeCoursey, C., Egami, E., Pierel, J. D. R., et al. 2025, 979, 250
- Drakos, N. E., Villaseñor, B., Robertson, B. E., et al. 2022, 926, 194
- Filippenko, A. V., Richmond, M. W., Branch, D., et al. 1992, *AJ*, 104, 1543, <https://ui.adsabs.harvard.edu/#abs/1992AJ....104.1543F/abstract>
- Fitzpatrick, E. L. 1999, 111, 63
- Foley, R. J., Challis, P. J., Chornock, R., et al. 2013, *ApJ*, 767, 57, <http://stacks.iop.org/0004-637X/767/i=1/a=57?key=crossref.be847ca54941021d2dbe7cb5b7ddacc5>
- Gal-Yam, A., & Leonard, D. C. 2009, 458, 865
- Gomez, S. 2023, Implementation of Unevenly Spaced Resultants in Pandeia, Nancy Grace Roman Space Telescope Technical Reports, 8 pp.
- Gomez, S., Berger, E., Nicholl, M., et al. 2019, 881, 87
- González-Gaitán, S., Perrett, K., Sullivan, M., et al. 2011, 727, 107
- González-Gaitán, S., Hsiao, E. Y., Pignata, G., et al. 2014, 795, 142
- Graur, O., Zurek, D. R., Rest, A., et al. 2017, arXiv:1711.01275, <http://arxiv.org/abs/1711.01275>
- Guillochon, J., Nicholl, M., Villar, V. A., et al. 2018, 236, 6
- Guy, J., Sullivan, M., Conley, A., et al. 2010, *A&A*, 523, A7, <http://www.aanda.org/10.1051/0004-6361/201014468>
- Harris, C. R., Millman, K. J., van der Walt, S. J., et al. 2020, *Nature*, 585, 357, <https://www.nature.com/articles/s41586-020-2649-2>
- Hinton, S., & Brout, D. 2020, *JOSS*, 5, 2122, <https://joss.theoj.org/papers/10.21105/joss.02122>
- Hounsell, R., Scolnic, D., Foley, R. J., et al. 2018, *ApJ*, 867, 23, <http://arxiv.org/abs/1702.01747>
- Hounsell, R., Scolnic, D., Brout, D., et al. 2023, arXiv e-prints, arXiv:2307.02670
- Hunter, J. D. 2007, *CSE*, 9, 90, <http://ieeexplore.ieee.org/document/4160265/>
- Inayoshi, K., Kashiyama, K., Li, W., et al. 2024, *ApJ*, 966, 164, <https://iopscience.iop.org/article/10.3847/1538-4357/ad344c>
- Jha, S. W. 2017, arXiv:1707.01110, <http://arxiv.org/abs/1707.01110>
- Jones, E., Oliphant, T., Peterson, P., et al. 2001, *Nature Methods*, arXiv:1907.10121, <http://www.scipy.org/>
- Kasen, D., & Bildsten, L. 2010, 717, 245
- Kasen, D., Metzger, B., Barnes, J., Quataert, E., & Ramirez-Ruiz, E. 2017, 551, 80
- Kasen, D., Woosley, S. E., & Heger, A. 2011, 734, 102
- Kessler, R., & Scolnic, D. 2017, *ApJ*, 836, 56, <http://stacks.iop.org/0004-637X/836/i=1/a=56?key=crossref.d0bddb5607f63ec4347f7e1b0143aef5>
- Kessler, R., Becker, A. C., Cinabro, D., et al. 2009a, *The Astrophysical Journal Supplement Series*, 185, 32, <http://stacks.iop.org/0067-0049/185/i=1/a=32?key=crossref.e6be94af96ce912e18d1d80a5ef79925>
- Kessler, R., Bernstein, J. P., Cinabro, D., et al. 2009b, *PASP*, 121, 1028, <http://iopscience.iop.org/article/10.1086/605984>
- Kessler, R., Narayan, G., Avelino, A., et al. 2019, *PASP*, 131, 094501, <https://iopscience.iop.org/article/10.1088/1538-3873/ab26f1>
- Kochanek, C. S. 2016, 461, 371
- Kozyreva, A., Kromer, M., Noebauer, U. M., & Hirschi, R. 2018, 479, 3106
- Li, W., Chornock, R., Leaman, J., et al. 2011a, 412, 1473
- Li, W., Filippenko, A. V., Chornock, R., et al. 2003, 115, 453
- Li, W., Leaman, J., Chornock, R., et al. 2011b, 412, 1441
- Lokken, M., Gagliano, A., Narayan, G., et al. 2023, *Monthly Notices of the Royal Astronomical Society*, 520, 2887, <https://academic.oup.com/mnras/article/520/2/2887/7010761>
- Madau, P., & Dickinson, M. 2014, *Annu. Rev. Astron. Astrophys.*, 52, 415, <https://www.annualreviews.org/doi/10.1146/annurev-astro-081811-125615>
- McCrum, M., Smartt, S. J., Rest, A., et al. 2015, 448, 1206
- McKinney, W. 2010, *Data Structures for Statistical Computing in Python*, <http://conference.scipy.org/proceedings/scipy2010/mckinney.html>
- Miller, A. A., Cao, Y., Piro, A. L., et al. 2017, arXiv:1708.07124, <http://arxiv.org/abs/1708.07124>
- Mockler, B., Guillochon, J., & Ramirez-Ruiz, E. 2019, 872, 151
- Moriya, T. J., Quimby, R. M., & Robertson, B. E. 2022, 925, 211
- Mosby, G., Rauscher, B. J., Bennett, C., et al. 2020, *Journal of Astronomical Telescopes, Instruments, and Systems*, 6, 046001
- Nicholl, M., Guillochon, J., & Berger, E. 2017, 850, 55
- Observations Time Allocation Committee, R., & Community Survey Definition Committees, C. 2025, arXiv e-prints, arXiv:2505.10574
- OpenUniverse, Collaboration, T. L. D. E. S., Team, T. R. H. P. I., Team, T. R. R. P. I., & Team, T. R. S. C. P. I. 2025, *MNRAS*, submitted
- Pan, T., Kasen, D., & Loeb, A. 2012, 422, 2701

- Pierel, J. D. R., Jones, D. O., Kenworthy, W. D., et al. 2022, 939, 11
- Pierel, J. D. R., Engesser, M., Coulter, D. A., et al. 2024, 971, L32
- Pierel, J. D. R., Coulter, D. A., Siebert, M. R., et al. 2025, 981, L9
- PLAsTiCC Modelers. 2022, Libraries & Recommended Citations for Using PLAsTiCC Models, <https://doi.org/10.5281/zenodo.6672739>, doi:10.5281/zenodo.6672739
- Popovic, B., Brout, D., Kessler, R., & Scolnic, D. 2021a, arXiv e-prints, arXiv:2112.04456
- Popovic, B., Brout, D., Kessler, R., Scolnic, D., & Lu, L. 2021b, *The Astrophysical Journal*, 913, 49, <https://ui.adsabs.harvard.edu/abs/2021ApJ...913...49P/abstract>
- Prajs, S., Sullivan, M., Smith, M., et al. 2017, 464, 3568
- Qu, H., Sako, M., Möller, A., & Doux, C. 2021, *AJ*, 162, 67, <https://iopscience.iop.org/article/10.3847/1538-3881/ac0824>
- Quimby, R. M., Yuan, F., Akerlof, C., & Wheeler, J. C. 2013, 431, 912
- Quimby, R. M., Kulkarni, S. R., Kasliwal, M. M., et al. 2011, 474, 487, <http://www.nature.com/doi/10.1038/nature10095>
- Rees, M. J. 1988, 333, 523
- Rose, B. M., Baltay, C., Hounsell, R., et al. 2021, arXiv:2111.03081, arXiv:2111.03081, <http://arxiv.org/abs/2111.03081>
- Rubin, D., Aldering, G., Astraatmadja, T. L., et al. 2022, arXiv e-prints, arXiv:2206.10632
- Rubin, D., Aldering, G., Betoule, M., et al. 2023, arXiv e-prints, arXiv:2311.12098
- Sánchez, B. O., Brout, D., Vincenzi, M., et al. 2024, *The Dark Energy Survey Supernova Program: Light Curves and 5-Year Data Release*, <http://arxiv.org/abs/2406.05046>, arXiv:2406.05046
- Sartori, L. F., Trakhtenbrot, B., Schawinski, K., et al. 2019, 883, 139
- Schlaflly, E. F., & Finkbeiner, D. P. 2011, *The Astrophysical Journal*, 737, 103, <http://stacks.iop.org/0004-637X/737/i=2/a=103?key=crossref.ac2fc76228f37d377c90dc70a3690b53>
- Schulze, S., Fransson, C., Kozyreva, A., et al. 2024, 683, A223
- Scolnic, D., Brout, D., Carr, A., et al. 2021, arXiv:2112.03863, <http://arxiv.org/abs/2112.03863>
- Shen, Y. 2013, *Bulletin of the Astronomical Society of India*, 41, 61
- Spergel, D., Gehrels, N., Baltay, C., et al. 2015, arXiv:1503.03757, <https://ui.adsabs.harvard.edu/abs/2015arXiv150303757S>
- Strolger, L.-G., Rodney, S. A., Pacifici, C., Narayan, G., & Graur, O. 2020, *ApJ*, 890, 140, <https://iopscience.iop.org/article/10.3847/1538-4357/ab6a97>
- Strolger, L.-G., Dahlen, T., Rodney, S. A., et al. 2015, 813, 93
- The PLAsTiCC team, Allam, Tarek, Jr., Bahmanyar, A., et al. 2018, arXiv e-prints, arXiv:1810.00001
- Van Der Wel, A., Franx, M., Van Dokkum, P. G., et al. 2014, *ApJ*, 788, 28, <https://iopscience.iop.org/article/10.1088/0004-637X/788/1/28>
- van Velzen, S. 2018, 852, 72
- Villar, V. A., Berger, E., Metzger, B. D., & Guillochon, J. 2017, 849, 70
- Vincenzi, M., Sullivan, M., Firth, R. E., et al. 2019, 489, 5802
- Vincenzi, M., Sullivan, M., Graur, O., et al. 2021, 505, 2819
- Vincenzi, M., Brout, D., Armstrong, P., et al. 2024, *The Dark Energy Survey Supernova Program: Cosmological Analysis and Systematic Uncertainties*, <http://arxiv.org/abs/2401.02945>, arXiv:2401.02945
- Wang, K. X., Scolnic, D., Troxel, M. A., et al. 2023, 523, 3874
- Waskom, M., Botvinnik, O., Ostblom, J., et al. 2020, *Zenodo*, doi:10.5281/zenodo.592845
- Weigel, A. K., Schawinski, K., Caplar, N., et al. 2017, *ApJ*, 845, 134, <https://dx.doi.org/10.3847/1538-4357/aa803b>
- Wiseman, P., Sullivan, M., Smith, M., et al. 2021, *Monthly Notices of the Royal Astronomical Society*, stab1943, <https://academic.oup.com/mnras/advance-article/doi/10.1093/mnras/stab1943/6318383>
- Wood-Vasey, W. M., Miknaitis, G., Stubbs, C. W., et al. 2007, 666, 694

Table 5. Description of `hourglass_objects.parquet`

Column Name	Description Name	Units	Type
<code>cid</code>	Candidate ID	...	integer
<code>field</code>	Field name	...	string
<code>class</code>	Object classification name	...	string
<code>sub_class</code>	Name of subclass, such as “IIP” or “Ic”	...	string
<code>z_cmb</code>	Redshift in CMB frame	...	float
<code>ra</code>	Right Ascension	degrees	float
<code>dec</code>	Declination	degrees	float
<code>mw_ebv</code>	Milky-way $E(B - V)$ along line-of-sight	AB mag	float
<code>peak_mjd</code>	Modified Julian date of maximum	...	float
<code>snr_max_Y</code>	Simulated peak S/N in Y -band	...	float
<code>snr_max_J</code>	Simulated S/N magnitude in J -band	...	float
<code>peak_mag_Y</code>	Simulated peak magnitude in Y -band	AB mag	float
<code>peak_mag_J</code>	Simulated peak magnitude in J -band	AB mag	float
<code>n_obs</code>	Number of total observations	...	integer
<code>t_rest_min</code>	Phase of first observation	days	float
<code>t_rest_max</code>	Phase of last observation	days	float
<code>scone_prob_Ia</code>	Probability of being a SN Ia via SCONE	...	float

APPENDIX

A. DATA RELEASE

The data is available at <https://doi.org/10.5281/zenodo.14262943>. It comes in three parquet files: `hourglass_objects.parquet`, `hourglass_photometry.parquet`, and `hourglass_spectra.parquet`. In python, these files can be read with Pandas via the `.read_parquet()` method. PyArrow also has a `.read_parquet()` method. PyArrow’s method allows for the inspection of the file prior to importing the whole thing into memory. One useful thing is to inspect the metadata with `pq.ParquetFile('hourglass_objects.parquet').metadata.metadata`. This provides information like the version of the data set and the date it was produced.

The object file is one row per object. It has all the “object-level” information like RA, Decl, redshift, S/N at maximum, and other information. The full list of columns for this file can be seen in Table 5. For operations, we expect these data releases to be richer. We release this set of simulations to engage the community to determine what light curve features are most useful to include.

The next file is the photometry file. It has one row per flux measurement. Each row has the “CID”, for joining with the “CID” column in the object file. Each row also has the flux, band, PSF, sky noise, and other photometry measurements. The full list can be seen in Table 6.

Finally we provide the spectroscopic data. This file is one row per object per epoch. Each row has a “CID” for joining with the object table. The full list of columns in this table can be found in Table 7.

Table 6. Description of `hourglass_photometry.parquet`

Column Name	Description Name	Units	Type
<code>cid</code>	Candidate ID	...	integer
<code>mjd</code>	Modified Julian date of observation	...	float
<code>band</code>	Photometric band, one of R, Z, Y, J, H, or F	...	string
<code>phot_flag</code>	Photometric Flag, 0 is pass	...	integer
<code>fluxcal</code>	Calibrated flux, $\text{mag} = 27.5 - 2.5 \log_{10}(\text{"fluxcal"})$...	float
<code>fluxcal_err</code>	Poisson uncertainty on "fluxcal", sky+galaxy+source	...	float
<code>psf_nea</code>	PSF noise equivalent area	pixels	float
<code>sky_sig</code>	Sky noise	ADU/pixel	float
<code>read_noise</code>	Read noise	ADU/pixel	float
<code>zp</code>	Zero-point	AB mag	float
<code>zp_err</code>	Error on zero-point	AB mag	float
<code>sim_mag_obs</code>	Input model mag	AB mag	float

Table 7. Description of `hourglass_spectra.parquet`

Column Name	Description Name	Units	Type
<code>cid</code>	Candidate ID	...	int
<code>mjd</code>	Modified Julian date of observation	...	float
<code>t_expose</code>	Exposure time	seconds	float
<code>n_bin_lam</code>	Number of wavelength bins	...	int
<code>lam_min</code>	Low wavelength edge of spectral bin	angstroms	list of floats
<code>lam_max</code>	High wavelength edge of spectral bin	angstroms	list of floats
<code>flam</code>	Flux per wavelength bin	erg/s/\AA/cm^2	list of floats
<code>flam_err</code>	Error on "flam"	erg/s/\AA/cm^2	list of floats
<code>sim_flam</code>	Input or true flux	erg/s/\AA/cm^2	list of floats